

## Control of the Anodic Aluminum Oxide Barrier Layer Opening Process by Wet Chemical Etching

Catherine Y. Han,<sup>†,‡</sup> Gerold A. Willing,<sup>†,§</sup> Zhili Xiao,<sup>||</sup> and H. Hau Wang\*

Materials Science Division, Argonne National Laboratory, Argonne, Illinois 60439

Received January 19, 2006. In Final Form: October 18, 2006

In this work, it has been shown that, through a highly controlled process, the chemical etching of the anodic aluminum oxide membrane barrier layer can be performed in such a way as to achieve nanometer-scale control of the pore opening. As the barrier layer is etched away, subtle differences revealed through AFM phase imaging in the alumina composition in the barrier layer give rise to a unique pattern of hexagonal walls surrounding each of the barrier layer domes. These nanostructures observed in both topography and phase images can be understood as differences in the oxalate anion contaminated alumina versus pure alumina. This information bears significant implication for catalysis, template synthesis, and chemical sensing applications. From the pore opening etching studies, the etching rate of the barrier layer (1.3 nm/min) is higher than that of the inner cell wall (0.93 nm/min), both of which are higher than the etching rate of pure alumina layer (0.5–0.17 nm/min). The established etching rates together with the etching temperature allow one to control the pore diameter systematically from 10 to 95 nm.

### Introduction

Porous anodic aluminum oxide (AAO) membranes have attracted significant interest during recent years due to the fact that they are readily synthesized through a simple procedure and extremely useful in nanoscience studies. Pore diameter (10–300 nm) and pore–pore distance (25–500 nm) can be controlled over a narrow distribution range through proper selection of the type and concentration of electrolyte, applied anodization potential, and temperature.<sup>1–4</sup> Highly ordered, straight nanopores in hexagonally close-packed arrays with domain sizes of approximately  $2.5 \times 2.5 \mu\text{m}^2$  and aspect ratios as high as 1000 can be readily achieved. The pore–pore distance and barrier oxide layer thickness are mainly determined by the applied anodization potential, while the electrolyte pH determines the dissolution rate of aluminum oxide, which directly affects the resulting pore diameter.

The nanopores within the AAO membranes can be used as templates for fabricating various nanoscale structures. Nanowires of a variety of materials, including Ni,<sup>5</sup> Bi,<sup>6</sup> Au,<sup>7–9</sup> Ag,<sup>10</sup> Co,<sup>11</sup> ZnO,<sup>12</sup> Fe,<sup>13</sup> and Sb<sup>14</sup> with diameters of 60–200 nm, have been fabricated by electrodeposition into the nanopores. Carbon nanotubes<sup>15</sup> and boron nanowires<sup>16</sup> have been created in the

AAO nanopores by utilizing a chemical vapor deposition technique. Highly ordered antidot arrays have also been produced by coating the surfaces of porous AAO membranes with magnetic<sup>17</sup> or superconducting<sup>18</sup> materials.

A hemispherical shell with homogeneous thickness known as the barrier layer develops at the bottom of every nanopore during the anodization process. To date, this barrier layer has not attracted much attention in the literature, even though many applications require its removal to create through-hole membranes. Examples for such applications include energy-efficient gas separation and pattern-transfer masks for e-beam evaporation,<sup>19</sup> reactive ion etching,<sup>20</sup> or molecular-beam epitaxial growth.<sup>21</sup> Through a carefully controlled barrier layer etching process, one can systematically prepare a tunable pore opening. Three methods had been used to open the barrier oxide layer: wet chemical etching,<sup>1–3</sup> ion milling,<sup>22</sup> and plasma etching.<sup>20</sup> Of these, the wet etching has been regarded as difficult to control and only ion milling has received more detailed analysis in the literature.<sup>22</sup>

Both ion milling and plasma etching have the advantage of maintaining intact pores after barrier layer removal, but require expensive equipment, and a typical setup allows only a small area around  $1 \times 1 \text{ mm}^2$  to be removed at any given time and, thus, they are cost- and time-intensive. Wet chemical etching, when properly controlled, can be used to etch samples with large dimensions (for example,  $2 \times 2 \text{ cm}^2$ ) and is fast, convenient, inexpensive, and reliable. It has been used routinely in our laboratory for opening the barrier layers of AAO membranes.

\* To whom correspondence should be addressed. E-mail: hau.wang@anl.gov.

<sup>†</sup> Equal contribution.

<sup>‡</sup> Current address: R.J. Daley College, Chicago, IL.

<sup>§</sup> Current address: Department of Chemical Engineering, University of Louisville, Louisville, KY.

<sup>||</sup> Current address: Department of Physics, Northern Illinois University, DeKalb, IL, and ANL/MSD.

- (1) Masuda H.; Satoh, M. *Jpn. J. Appl. Phys.* **1996**, *35*, L126.
- (2) Masuda, H.; Hasegawa, F.; Ono, S. *J. Electrochem. Soc.* **1997**, *144*, L127.
- (3) Masuda, H.; Yada, K.; Osaka, A. *Jpn. J. Appl. Phys.* **1998**, *37*, L1340.
- (4) Li, A. P.; Müller, F.; Birner, A.; Nielsch, K.; Gösele, U. *J. Appl. Phys.* **1998**, *84*, 6023.
- (5) Nielsch, K.; Müller, F.; Li, A.; Gösele, U. *Adv. Mater.* **2000**, *12* (8), 582.
- (6) Wang, X. F.; Zhang, L. D.; Zhang, J.; Shi, H. Z.; Peng, X. S.; Zheng, M. J.; Fang, J.; Chen, J. L.; Gao, B. J. *J. Phys. D: Appl. Phys.* **2001**, *34*, 418.
- (7) Wang, Z.; Su, Y. K.; Li, H. L. *Appl. Phys. A* **2002**, *74*, 563.
- (8) Brumlik, C. J.; Menon, V. P.; Martin, C. R. *J. Mater. Res.* **1994**, *9* (5), 1174.
- (9) Foss, C. A., Jr.; Hornyak, G. L.; Stockert, J. A.; Martin, C. R. *J. Phys. Chem.* **1994**, *98*, 2963.
- (10) Sauer, G.; Brehm, G.; Schneider, S.; Nielsch, K.; Wehrspohn, R. B.; Choi, J.; Hofmeister, H.; Gösele, U. *J. Appl. Phys.* **2002**, *91* (5), 3243.
- (11) Zeng, H.; Zheng, M.; Skomki, R.; Sellmyer, J.; Liu, Y.; Menon, L.; Bandyopadhyay, S. *J. Appl. Phys.* **2000**, *87* (9), 4718.

- (12) Li, Y.; Meng, G. W.; Zhang, L. D. *Appl. Phys. Lett.* **2000**, *76* (15), 2011.
- (13) Li, F.; Metzger, R.; Doyle, W. D. *IEEE Trans. Magn.* **1997**, *33* (5), 3715.
- (14) Zhang, Y.; Li, G.; Wu, Y.; Zhang, B.; Song, W.; Zhang, L. *Adv. Mater.* **2002**, *14* (17), 1227.
- (15) Li, J.; Papadopoulos, C.; Xu, J. M.; Moskovits, M. *Appl. Phys. Lett.* **1999**, *75* (3), 367.
- (16) Yang, Q.; Sha, J.; Xu, J.; Ji, Y. J.; Ma, X. Y.; Niu, J. J.; Hua, H. Q.; Yang, D. R. *Chem. Phys. Lett.* **2003**, *379*, 87.
- (17) Xiao, Z. L.; Han, C. Y.; Welp, U.; Wang, H. H.; Vlasco-Vlasov, V. K.; Kwok, W. K.; Miller, D. J.; Hiller, J. M.; Cook, R. E.; Willing, G. A.; Crabtree, G. W. *Appl. Phys. Lett.* **2002**, *81*, 2869.
- (18) Crabtree, G. W.; Welp, U.; Xiao, Z. L.; Jiang, J. S.; Vlasco-Vlasov, V. K.; Bader, S. D.; Liang, J.; Chik, H.; Xu, J. M. *Physica C* **2003**, *387*, 49.
- (19) Masuda, H.; Yasui, K.; Nishio, K. *Adv. Mater.* **2000**, *12* (14), 1031.
- (20) Liang, J.; Chik, H.; Yin, A.; Xu, J. J. *J. Appl. Phys.* **2002**, *91*, 2544.
- (21) Mei, X.; Kim, D.; Ruda, H. E.; Guo, Q. X. *Appl. Phys. Lett.* **2002**, *81*, 361.
- (22) Xu, T.; Zangari, G.; Metzger, R. M. *Nano Lett.* **2002**, *2*, 37.

While there seems to be a number of researchers utilizing chemical etching for opening the barrier layer, very little detailed study has been made in the past to reveal the barrier layer opening process. As such, there is a lack of knowledge concerning the dynamics of this process. The most common remark upon this process that can be found in the literature is "...the barrier layer is removed in 5% H<sub>3</sub>PO<sub>4</sub> at 30 °C for 60 min."<sup>1</sup> Our experimental results show that if the chemical etching is done with proper control, 10–95 nm openings in the barrier layer can be obtained systematically for AAO membranes made in oxalic acid. In addition, very interesting double hexagon nanostructures were observed for the first time through AFM imaging before complete removal of the barrier layer. These nanostructures reveal the impurity distribution in the membranes that bear significant implication for catalysis and sensing applications.

### Experimental Section

Anodic aluminum oxide (AAO) membranes with hexagonally ordered arrays of nanopores were prepared by a two-step anodization procedure as described previously.<sup>1</sup> Aluminum sheets (Alfa Aesar, 99.998% pure, 0.5 mm thick) were degreased in acetone and then annealed at 500 °C for 4 h under an argon atmosphere. The Al sheets were then electropolished in a solution of HClO<sub>4</sub> and ethanol (1:8, v/v) at a current density of 200 mA/cm<sup>2</sup> for 10 min or until a mirror-like surface smoothness was achieved.

The first anodization step was carried out in a 0.3 M oxalic acid solution at 3 °C for 24 h. The 70 μm thick porous alumina layer was then stripped away from the Al substrate by etching the sample in a solution containing 6 wt % phosphoric acid and 1.8 wt % chromic acid at 60 °C for 12 h. This step not only removes the disordered AAO membrane but also leaves a highly ordered dimple array on the aluminum surface. Each dimple initiates new pore formation during the second anodization step, which was carried out under the same conditions as the first step. A freestanding AAO membrane with highly ordered arrays of nanopores was then obtained by selectively etching away the unreacted Al in a saturated HgCl<sub>2</sub> solution.

A U-shaped aluminum oxide layer or barrier layer with a thickness of 30–40 nm forms at the bottom of every nanopore during anodization. A protective polymer layer made of a mixture of nitrocellulose and polyester resin was coated on the top surface of the AAO membrane that is opposite to the barrier layer to prevent overetching of the surface structure and uneven diffusion of acid into the nanopores.<sup>26</sup> The membrane was then immersed in 200 mL of 5.00 wt % phosphoric acid at 30.0 °C for different periods of time, rinsed with distilled water, and dried under ambient conditions. The barrier layer removal and pore widening process was then studied with use of AFM (Digital Instruments, Dimension 3000 with a type IIIa controller and TESP Si cantilevers) and SEM (Hitachi S-4700-II). Effective pore diameters were determined by analyzing the total pore area of each image using Scion Image based on NIH Image to ascertain the average area per pore and, hence, the average pore diameter.

### Results and Discussion

The model of an AAO nanopore is shown in Figure 1 by following a literature reference.<sup>25</sup> As indicated in the figure,  $C$  is the cell dimension (pore-to-pore distance) with cell wall thickness  $w$ ,  $P$  is the pore diameter, and  $A$  is the center of curvature that moves continuously during anodization toward the bottom. The active layer during nanopore growth is the barrier layer with thickness ( $d$ ). There are two active interfaces associated with the barrier layer. The outer one is associated with oxidation of

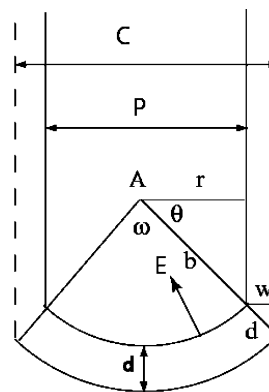


**Figure 1.** Schematic drawing of the cross section of a nanopore.

aluminum to aluminum cation ( $\text{Al} \rightarrow \text{Al}^{3+}$ ), and the inner one is associated with  $\text{O}^{2-}$  migration that leads to the formation of alumina ( $\text{Al}_2\text{O}_3$ ), as well as dissolution and deposition of alumina to and from the etching solution. The whole process is driven by the local electric field ( $E$ ), which is defined by the current applied ( $I$ ) over conductivity ( $\sigma$ ) and the surface area of the spherical bottom ( $\omega/4\pi \times 4\pi b^2 = \omega b^2$  where  $\omega$  is the solid angle of the active barrier area and  $b$  radius of curvature).

$$E = \frac{J}{\sigma} = \frac{I}{\sigma \omega b^2}$$

Under a constant applied potential and during equilibrium growth, each nanopore will reach an optimized solid angle  $\omega$  and radius of curvature  $b$ , which will lead to a consistent pore diameter and result in a two-dimensional hexagonally close-packed pore array.

**AAO Barrier Layer Opening** This study utilizes a freestanding AAO film with a protective polymer layer made of a mixture of nitrocellulose and polyester resin on the porous side of the film.<sup>26</sup> The polymer layer is used to block the pores and thus prevent uneven etching of the AAO barrier layer from inside, which may be caused by the uneven acid diffusion through the AAO pores. The presence of the protective layer also focuses the etching process on the bottom side of the barrier layer, which is comprised of a hexagonally close packed array of hemispherical domes that are 120 nm in diameter and 27 nm in height (Figure 2a). The domes begin to shrink both in diameter and height once the etching process starts. After 18 min of etching, the domes have decreased in size to approximately 100 nm in diameter and 24 nm in height (Figure 2b). It is interesting to note that, at this early stage of the etching process, the walls of each individual cell are becoming more pronounced, which suggests that the area in-between individual domes is not etched as quickly as the domes themselves. This trend continues through 30 min of etching with the domes continuing to decrease in size (85 nm in diameter and 16 nm in height) and the hexagonal cell walls becoming clearly visible to form a double hexagon nanostructure (Figure 2c).

After 40 min of etching, the barrier layer is finally breached by the acid (Figure 2d). Note that the initial opening is uneven across the surface. The majority of the cells have an opening of ~10 nm, while some of the cells remain closed. While the aluminum surface used to create the AAO membrane was annealed and electropolished before anodization, the surface still maintains a certain degree of roughness. This roughness translates into a subtle variation in the thickness of the barrier layer.<sup>23</sup> Those domes that are thinner would obviously be etched through earlier. It should also be noted that the walls of each individual

(23) Masuda, H.; Abe, A.; Nakao, M.; Yokoo, A.; Tamamura, T.; Nishio, K. *Adv. Mater.* **2003**, *15* (2), 161.

(24) Zhou, B.; Ramirez, W. F. *J. Electrochem. Soc.* **1996**, *143*, 619.

(25) O'Sullivan, J. P.; Wood, G. C. *Proc. R. Soc. London A* **1970**, *317*, 511.

(26) Xu, T. T.; Piner, R. D.; Ruoff, R. S. *Langmuir* **2003**, *19*, 1443.

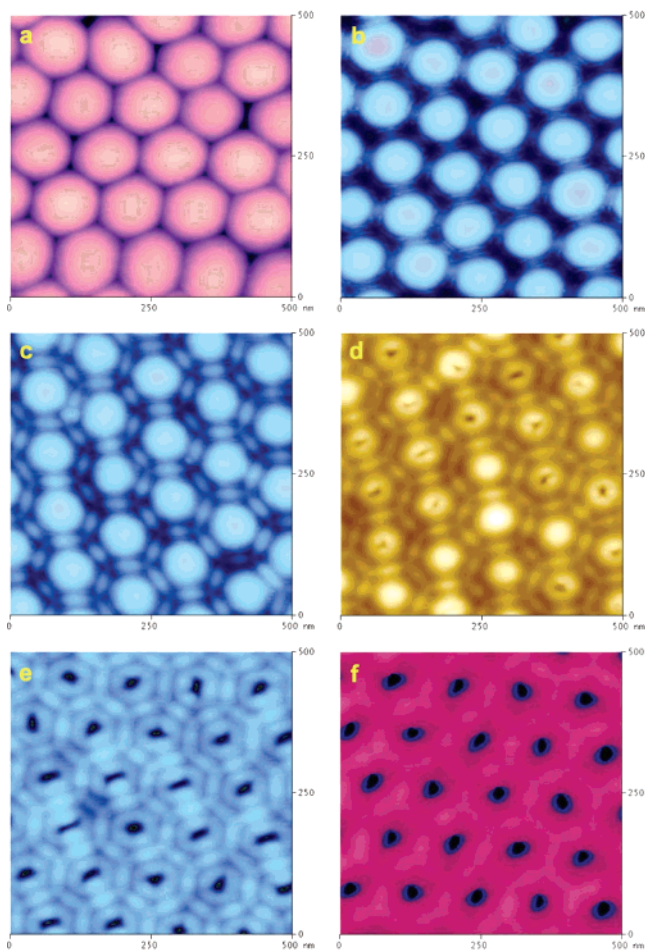


**Figure 2.** Stages of chemical etching process of the anodic aluminum oxide barrier layer. Etching progress after (a) 0 min, (b) 18 min, (c) 30 min, (d) 40 min, (e) 50 min, and (f) 60 min.

cell have become distinct enough to completely encircle each dome. Once the domes have been breached initially, the openings begin to widen to generate a unique surface topography which combines a hexagonal cell wall surrounding each opened dome. This process can be used to create membranes with a wide range of pore diameters with fixed pore-to-pore distance, from sub-10 nm, to 34 nm, to 48 nm, and to 70 nm just by terminating the etching process at 40, 50, 60, and 70 min, respectively (Figures 2d–2f and Figure 3a). The pronounced hexagonal walls persist through the entire procedure, even after the barrier layer has been completely removed at 70 min of etching.

As can be seen from the images, the pores become more circular as etching progresses. This is similar to other techniques, like ion milling, where the pore shape is fairly circular at larger pore diameters (ca. 45 nm) but some distortion is still observed.<sup>22</sup> While these images may represent the true shape of the hole, especially at the smaller diameters, there is also the possibility that there is a convolution between the AFM tip and hole that is distorting the image. We suspect that this is partially the case as there were some changes in the image depending on the scan direction, which is a clear indication that tip shape is affecting the image. Even if this is the case though, these results suggest that applications that require a very uniform shape should utilize membranes that have been etched for longer periods of time to ensure a more uniform pore shape.

**Two Regions of Different Etching Rates** Figure 4 shows the rate of pore opening as a plot of pore diameter with respect to time measured by AFM (○) and SEM (●) imaging. The effective

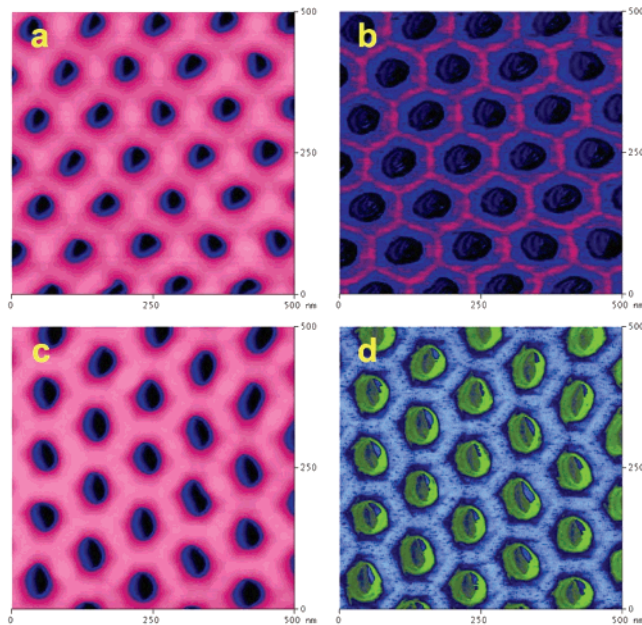


**Figure 3.** AFM topography and phase images of the AAO membrane after (a and b) 70 min and (c and d) 90 min of etching.

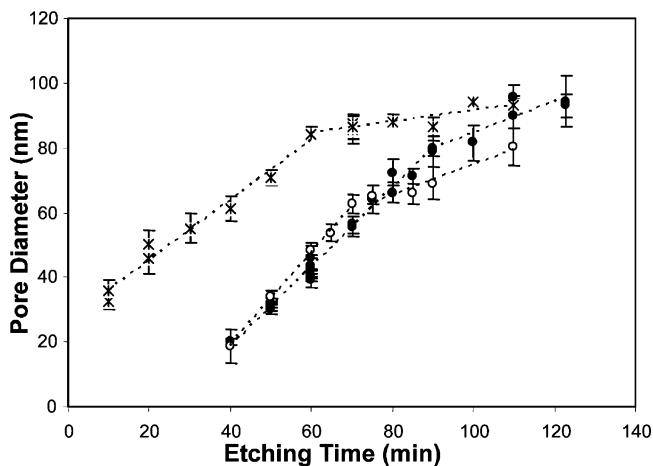


**Figure 4.** Etching of the barrier side (●, SEM; ○, AFM) and front side (\*, SEM) of AAO membranes in 5.00 wt %  $\text{H}_3\text{PO}_4$  at 30.0 °C.

diameter at each time step is obtained from the average pore area measured over a large number of pores across several sample membranes. Note that the two techniques give fairly consistent results, especially before the complete removal of the barrier layer. From 40 to 90 min of etching, the pore opening rate is about 1.3 nm/min, but the following pore expansion rate is much slower, at about 0.5 nm/min. A variation in the diffusion rate of acid across the surface can be ruled out as a cause of this etching rate difference as there is very little height variation initially from the top of the dome to the bottom of the crevice, as can be seen in Figure 5a. This means the barrier layer must consist of materials that are more susceptible to chemical etching than the materials building the inner cell wall of the AAO pore. We attribute this to the fact that the barrier layer is the growth front of the anodization process;<sup>25</sup> it is constantly building up and redissolving. This action allows the oxalate anion ( $\text{Ox}$ ),  $\text{C}_2\text{O}_4^{2-}$ , and  $\text{H}_2\text{O}$  to be mixed with the alumina within the barrier layer, leading to a less dense composite material,  $\text{Al}_2\text{O}_3$  mixed with  $\text{Al}_2(\text{Ox})_3$ .

To further verify that there is a material difference between the domes and the cell walls, we carried out an etching experiment on the front side of an AAO membrane under the same conditions.

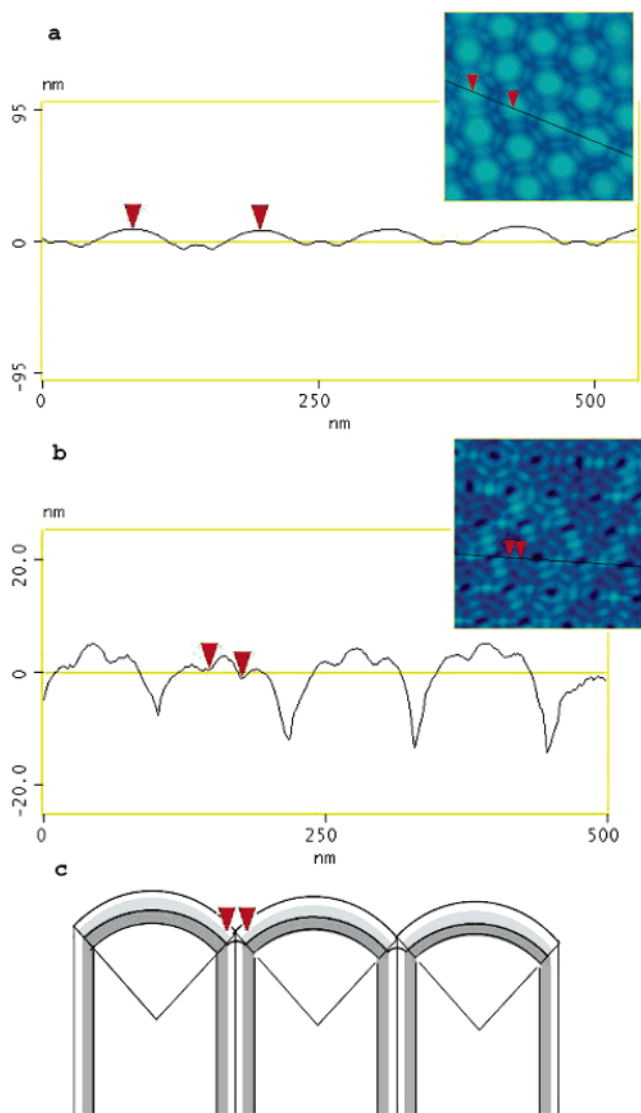


**Figure 5.** (a) Section analysis of AAO membrane at 30 min etching (same sample as Figure 2c) showing a cross section of the barrier layer and the double-dip feature. (b) Section analysis of AAO membrane at 50 min etching (same as Figure 2e) showing the collapsed dome and the double-dip feature (marked with red arrows). (c) Schematic drawing of the bilayered cell wall (gray area, oxalate contaminated alumina; white, pure alumina), the barrier layer (shown with thicker oxalate contaminated layer), and the double-dip feature observed during etching.

The results, as seen in Figure 4 (\*, measured by SEM), show that there are also two different regimes. The first regime, which runs from 10 to 60 min, shows the pore diameter increasing at a rate of 0.93 nm/min, which means the cell walls are etched at a slower rate than the domes of the barrier layer (1.3 nm/min). As can be seen from Figure 4, the change in diameter versus time is fairly linear. The second regime, which begins at 60 min, has an etching rate of only 0.17 nm/min. The two different etching rates clearly indicate that the cell wall is comprised of two different material layers. Earlier studies of AAO have suggested that there is a measurable difference in the alumina of these two areas arising from the entrapment of conjugated base anions in the alumina near the pore.<sup>27</sup> During our recent qualitative UV-Raman studies pure alumina powders, AAO membrane prepared from oxalic acid, and commercial dehydrated aluminum oxalate were compared.<sup>28</sup> While pure amorphous alumina gave no Raman band in the 600–1900  $\text{cm}^{-1}$  region, the AAO membrane and  $\text{Al}_2(\text{Ox})_3$  revealed nearly the same UV-Raman spectra. The inner

layer consists of oxalate  $\text{C}_2\text{O}_4^{2-}$  anion contaminated alumina while the outer layer consists of relatively pure alumina.<sup>27</sup> The ion mobility,  $\mu$ , is the limiting velocity of an ion ( $v$ ) in an electric field ( $E$ ) of unit strength. The force from the field to the ion is  $|z|eE$  which is balanced by the frictional drag that can be approximated by Stokes law,  $6\pi\eta rv$ , where  $z$  is the charge on the ion,  $e$  the electronic charge,  $\eta$  the viscosity of the medium, and  $r$  the radius of the ion.<sup>29</sup> Combining the two formulas gives

$$\mu = \frac{v}{E} = \frac{|z|e}{6\pi\eta r} = A \frac{|z|}{r}$$

The mobility ratio of oxygen anion to oxalate anion can be estimated from their radii:  $\mu_{\text{O}^{2-}}/\mu_{\text{C}_2\text{O}_4^{2-}} = r_{\text{C}_2\text{O}_4^{2-}}/r_{\text{O}^{2-}} \sim 1.8$ . Therefore, only the inner layer of the cell wall is contaminated with the oxalate anions due to their much slower mobility and it is reasonable that the anion contaminated alumina is easier to be etched away by  $\text{H}_3\text{PO}_4$  than the purer alumina, as shown by our etching rate studies.

**Underlying Structure and Impurity Distribution.** Knowing about the presence of pure alumina and oxalate contaminated alumina and identifying two different etching rates, the double hexagon nanostructures observed between 18 min (Figure 2b) and 60 min (Figure 2f) etching time can now be analyzed in more detail. These unique nanostructures can only be observed during this  $\sim 40$  min window and have never been reported previously. Figures 5a and 5b show the section analyses of the AAO membranes just before (30 min etching) and after (50 min) the barrier layer was breached, respectively. The double-dip features with 25 nm separation and 2.5 nm height at the 30 min etching (Figure 5a) and 31 nm separation and 2.9 nm height at the 50 min etching (marked in Figure 5b) are clearly observed in both figures and indicate the boundary of pure alumina between the cells as depicted schematically in Figure 5c. In addition, the two types of alumina as indicated in the cell wall of Figure 5c can be observed from the AFM phase imaging technique, which is sensitive to changes in elastic modulus and surface hardness of the AAO membrane. The cell wall nanostructures can be observed from both topography (Figure 2c–2f) and phase imaging (not shown here). At the early etching stage (18 min, Figure 2b) and just after the barrier layer has been removed (70 min, Figure 3a), while topography imaging simply showed the actual cell size and shape, phase imaging continued to reveal the underlying cell wall nanostructures. As shown in pseudo color (Figure 3b, 70 min), the contaminated alumina is indicated with light blue next to the dark blue pore, while the pure alumina of the cell wall, which is harder than the alumina near the pore, is indicated as pink. As the pores are etched further (90 min etching, Figure 3c), this contaminated layer is quickly removed, leaving behind only the pure alumina wall indicated as blue walls in Figure 3d and empty pores in green.

**Implications of the Barrier Layer.** If the barrier layer was made of concentric layers of the same material throughout the whole curvature, the whole barrier layer should be etched away all at once under homogeneous etching without diffusion limit, which is not supported by the aforementioned observation. It is quite obvious from Figure 2d–2f that the barrier layer is first breached at the very top or center of the domes, and then the small opening is gradually enlarged and eventually the whole

(27) Thompson, G. E.; Wood, G. C. *Nature* **1981**, 290, 230.

(28) Xiong, G.; Elam, J. W.; Feng, H.; Han, C. Y.; Wang, H. H.; Iton, L. E.; Curtiss, L. A.; Pellin, M. J.; Kung, M.; Kung, H.; Stair, P. C. *J. Phys. Chem. B* **2005**, 109, 14059.

(29) Bard, A. J.; Faulkner, L. R. *Electrochemical Methods Fundamentals and Applications*; John Wiley & Sons: New York, 1980; p 65.

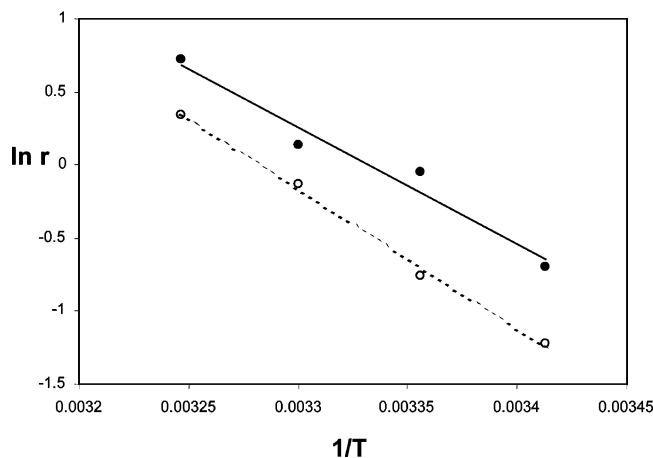


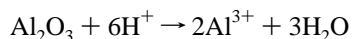
**Figure 6.** Reaction rates before (○) and after (●) breaching of the barrier layer at four different temperatures (20, 25, 30, and 35 °C).

dome is etched away as the chemical etching process proceeds. Based on our etching results, the barrier layer cannot consist of simple concentric layers with different purity. The barrier layer is more complex than the composition of the bilayer cell wall. From the breaching pattern, the impure inner layer is thicker around the center of each barrier layer. This is possibly due to the fact that anodization is a dynamic process. Since the effective center of curvature is continuously moving forward during anodization, the center area of each cell barrier always remains redox active while the boundary between the bottom barrier and cell wall is gradually becoming redox inactive. There are two resulting effects from this transition. First, the barrier layer will contain more oxalate anions than that of the cell wall as evidenced by the faster etching rate (Figure 4 barrier vs front etching). Second, while migration of the oxalate anions driven by an electric field will stop after the boundary area becomes inactive, diffusion of oxalate from the barrier layer to the cell wall due to higher concentration will continue. This process would leave the boundary of the barrier with a lower oxalate concentration and the center of the barrier layer a slightly higher oxalate concentration. While this hypothesis explains the phenomenological observation of a pore opening, quantitative explanation must rely on detailed theoretical simulation which is beyond the scope of this study.

**Temperature Dependency of the Etching Rate.** The reaction rates before and after the breaching of the barrier layer were measured at four different temperatures (20, 25, 30, and 35 °C) in 5.00 wt %  $\text{H}_3\text{PO}_4$ . Assuming that the rate constant,  $k$ , obeys the Arrhenius temperature dependence, the rate ( $r$ ) leads to

$$r = Ae^{-E/RT}[\text{H}^+]$$

This equation assumes that the reaction rate is first order with respect to the hydrogen ion concentration. While this would not seem obvious from the equation for the etching reaction,



prior work has shown that the rate law is first-order.<sup>24</sup> Plotting  $\ln r$  versus  $1/T$  (Figure 6) gives the relationship of reaction rate and etching temperature as

$$\ln r_{\text{before}} = -9600 \times (1/T) + 32 \quad (R^2 = 0.9963)$$

$$\ln r_{\text{after}} = -8000 \times (1/T) + 27 \quad (R^2 = 0.963)$$

The activation energy for etching before pore opening is  $\sim 20\%$  higher and the correlations can be used to calculate the reaction

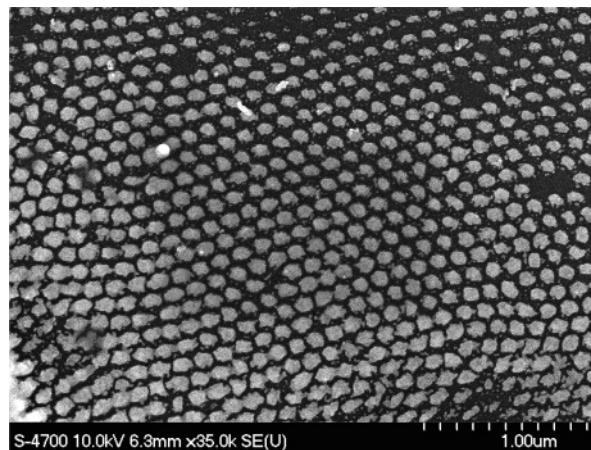


**Figure 7.** SEM image of a Au nanodot array on a silicon wafer (90 nm dot diameter and 125 nm dot-to-dot distance). The missing Au dots may be the results of pore blockage or loss during the mask lift-off process.

rate at any given temperature and thus can be used to predict the approximate etching time to achieve a desired pore diameter.

**Demonstration as a Nanomask.** AAO membranes with various pore diameters are useful for mask applications. As a simple demonstration, we prepared a thin AAO membrane (750 nm thick) with the pore (90 nm) completely open and placed the AAO mask over a Si wafer. Through thermal evaporation, a 50 nm Au thin film was deposited on the AAO membrane. The alumina membrane was then removed with chemical etching and the resulting 50 nm Au nanodot array on Si is shown in Figure 7. These Au nanodots are deposited in a hexagonally close-packed pattern exactly mirroring the AAO pore arrangement. The whole process, which demonstrates the proof of concept, was carried out in a wet chemistry lab setting and no lithographic tools were required. The missing regions of dots are most likely due to the fact that the masking process has not been optimized and as such, some areas of the gold did not fully adhere to the Si substrate prior to removal of the AAO mask. Further studies into the masking process should improve the yield and uniformity of the nanodot array. These metallic nanodot arrays can be used in the future for chemical sensing and localized surface plasmon resonance Raman enhancement studies.

## Summary

In this work, it has been shown that through a highly controlled process the chemical etching of the AAO barrier layer can be performed in such a way as to achieve nanometer scale control of the pore opening. Such control can be extremely useful in membrane technology and lithographic mask applications. Also, as the barrier layer is etched away, subtle differences revealed through AFM phase imaging in the alumina composition in the barrier layer give rise to a unique pattern of hexagonal walls surrounding each of the barrier layer domes. In addition, the oxalate anion contaminated alumina and pure alumina in these membranes have been directly imaged with AFM techniques. This information bears significant implication for future catalysis, template synthesis, and chemical sensing applications.

**Acknowledgment.** Work at Argonne National Laboratory is sponsored by the U.S. Department of Energy, Office of Basic Energy Science, Division of Materials Science, under Contract W-31-109-ENG-38. C.Y.H. and H.H.W. acknowledge the use of the ANL/EMC facility. G.A.W. and H.H.W. acknowledge the use of the ANL/MSD AFM facility.